nature physics

ARTICLES

PUBLISHED ONLINE: 15 AUGUST 2016 | DOI: 10.1038/NPHYS3842

Anti-parity–time symmetry with flying atoms

Peng Peng[1], Wanxia Cao[1], Ce Shen[1], Weizhi Qu[1], Jianming Wen[2]*, Liang Jiang[2]* and Yanhong Xiao[1,3]*

The recently developed notion of parity–time (PT) symmetry in optical systems has spawned intriguing prospects. So far, most experimental implementations have been reported in solid-state systems. Here, we report the first experimental demonstration of optical anti-PT symmetry—the counterpart of conventional PT symmetry—in a warm atomic-vapour cell. Rapid coherence transport via flying atoms leads to a dissipative coupling between two long-lived atomic spin waves, allowing for the observation of the essential features of anti-PT symmetry with unprecedented precision on the phase-transition threshold, as well as refractionless light propagation. Moreover, we show that a linear or nonlinear interaction between the two spatially separated beams can be achieved. Our results advance non-Hermitian physics by bridging to the field of atomic, molecular and optical physics, where new phenomena and applications in quantum and nonlinear optics aided by (anti-)PT symmetry could be anticipated.

Canonical quantum mechanics postulates Hermitian Hamiltonians, to describe closed physical systems, to ensure real eigenvalues and the orthonormality between eigenstates with different eigenenergies. For open systems, non-Hermitian Hamiltonians with complex eigenvalues and non-orthogonal eigenfunctions are commonly expected. However, such an understanding has been radically challenged since a counterintuitive discovery by Bender and Boettcher in 1998[1], where a wide class of non-Hermitian Hamiltonians (H), subject to $[H, \hat{P}\hat{T}]=0$ with the parity–time (PT) operator ($\hat{P}\hat{T}$), could display entirely real spectra below some threshold. More strikingly, a sharp, symmetry-breaking transition occurs once a non-Hermitian parameter crosses an exceptional point. This pioneering work immediately stimulated considerable theoretical efforts in extending Hermitian quantum theory to non-Hermitian systems[2–4]. Unfortunately, quantum mechanics is, by nature, Hermitian and, thus, any attempt to observe PT symmetry under such a theoretical framework is out of reach. Thanks to the mathematical isomorphism between the quantum Schrödinger and paraxial wave equations, a PT-symmetric complex potential can be readily established by judiciously making use of refractive indices with balanced gain and loss[5] in an optical setting. This suggests optics as a fertile ground for experimental investigations on PT symmetry without introducing any conflict with standard quantum mechanics. Optical realizations[6–14] have motivated various synthetic designs with peculiar properties otherwise unattainable in traditional Hermitian structures, including band merging[5], double refraction[15], unidirectional propagation[7,10,16–18], and power oscillation[7,19]. Other designs include coherent perfect laser absorbers[11,20,21], optical switches[22], optical couplers[23], and single-mode amplifiers[14,24]. Inspired by optical settings, systems using plasmonics[25], LRC circuits[26], acoustics[27], artificial lattices[28] and optomechanics[29] have also been reported.

As a counterpart, an anti-PT-symmetric Hamiltonian follows $\{H, \hat{P}\hat{T}\} = 0$. Mathematically, a conventional PT-symmetric Hamiltonian would become anti-PT-symmetric on multiplying by 'i', implying properties of anti-PT systems conjugate to those of PT systems. For instance, in the symmetry-unbroken regime, lossless propagation in a PT system corresponds to refractionless (or unit-refraction) propagation in an anti-PT system. Such an intriguing effect may open up new opportunities for manipulating light and form a complementary probe in non-Hermitian optics. Despite the appealing features, the realization of anti-PT symmetry is both theoretically and experimentally challenging. We notice that the first theoretical proposal[30] relies on a composite system of metamaterials by demanding an impractical balance of positive and negative real refractive indices in space. A subsequent extension considers an optical lattice of spatially driven cold atoms[31]. Notably, theoretical proposals[32–34] using cold atoms for PT symmetry have already been put forward in the spatial domain. Indeed, coherently prepared multilevel atoms are attractive systems for exploring non-Hermitian physics, because of their easy reconfiguration, flexible tunability, and especially the various coherence control techniques enabled by electromagnetically induced transparency (EIT)[35–40]. However, such an experiment has yet to be performed, primarily due to the hurdle of creating PT- or anti-PT-symmetric optical potentials through the rather complicated spatial modulation of driving fields or optical lattices.

In this article, we report the first experimental realization of anti-PT-symmetric optics by introducing a novel coupling mechanism. The coupling between two spatially separated probe fields is mediated through coherent mixing of spin waves created in two parallel optical channels, in contrast to existing PT experiments where two optical fields of interest are coupled directly. Two spin waves here are mixed through coherently diffusing atomic ground-state coherence carried by moving atoms. The spin-wave coupling enables either linear or nonlinear interactions between the two probe fields. Also, the precise measurement on (anti-)PT phase transition in the frequency domain differentiates our work from former work rooted on either solid-material or (theoretical) cold-atomic systems. The characteristic of easy controllability further renders the scheme as an alternative stage for probing non-Hermitian physics related to the exceptional point[41–46].

Our experiments (schematically shown in Fig. 1a) are carried out in a ^{87}Rb vacuum vapour cell of cylindrical shape, with a diameter of 2.5 cm and length 5 cm. The inner surface of the cell is coated by coherence-preserving paraffin[47], which allows atoms to undergo thousands of wall collisions with little demolition of their internal quantum state. For comparisons between experiment and theory, an optically thin medium is preferable with the cell temperature set at ∼40 °C. The cell is housed within a four-layer magnetic shield to

[1]Department of Physics, State Key Laboratory of Surface Physics, and Key Laboratory of Micro and Nano Photonic Structures (Ministry of Education), Fudan University, Shanghai 200433, China. [2]Department of Applied Physics, Yale University, New Haven, Connecticut 06511, USA. [3]Collaborative Innovation Center of Advanced Microstructures, Nanjing 210093, China. *e-mail: jianming.wen@yale.edu; liang.jiang@yale.edu; yxiao@fudan.edu.cn

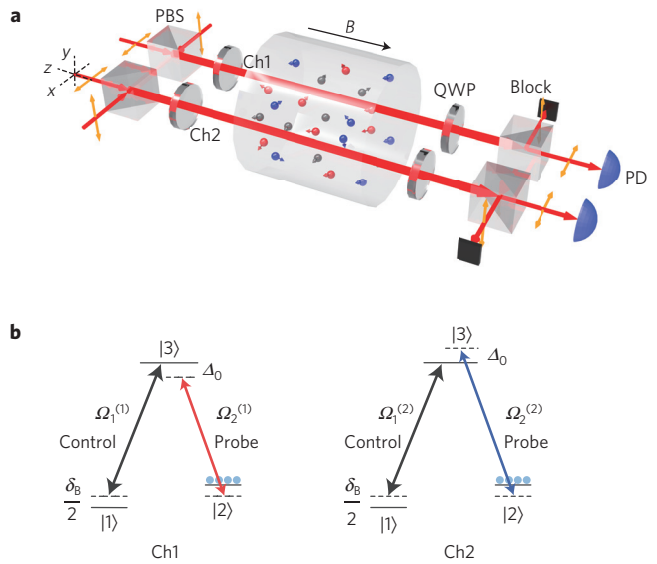

Figure 1 | Anti-PT-symmetric optics via rapid atomic-coherence transport in a warm ^{87}Rb vapour cell. a, Schematic of a three-dimensional view of the system. Two spatially separated optical channels (Ch1 and Ch2) each contain collinearly propagating weak-probe and strong-control fields operating under the condition of EIT. Ballistic atomic motion in a paraffin-wall-coated vacuum cell distributes atomic coherence through the optically thin medium and results in effective coupling between the two optical channels. With the temperature maintained at 40 °C, the cell is housed within a four-layer magnetic shield to screen out the ambient magnetic field. Output probe transmission spectra are measured by sweeping a homogeneous magnetic field generated by a solenoid inside the shield. PD, photodetector. **b**, The implementation of anti-PT symmetry utilizing standard three-level Λ-type EIT configurations in two channels, where the two ground states are Zeeman sublevels $|F=2, m_F=0\rangle$ and $|F=2, m_F=2\rangle$, and the excited state is $|F'=1, m_{F'}=1\rangle$ of the ^{87}Rb D_1 line. An external cavity diode laser provides the light for the probe and control fields with orthogonal circular polarizations. Right-circularly polarized strong-control fields, $\Omega_1^{(1)}$ and $\Omega_1^{(2)}$ in Ch1 and Ch2 are, respectively, on resonance with the transition $|1\rangle \rightarrow |3\rangle$; while left-circularly polarized weak-probe fields, $\Omega_2^{(1)}$ and $\Omega_2^{(2)}$ in Ch1 and Ch2, are near resonant with $|2\rangle \rightarrow |3\rangle$, but frequency shifted in opposite directions by the same amount $|\Delta_0|$, with Δ_0 being the difference between the probe and the control field frequencies. At steady state, the population is mainly in the ground state $|2\rangle$.

screen out the ambient magnetic field. Inside the shield a solenoid is used to generate a uniform magnetic field, inducing a Zeeman shift δ_B to the two-photon detuning. The laser beam, derived from an external cavity diode laser operating at the ^{87}Rb D_1 line (795 nm), is spatially split into four beams (1.2 mm in diameter) using half-wave plates and polarization beam splitters (PBS). Orthogonally linearly polarized probe and control beams are recombined, converted to circular polarization by quarter-wave plates (QWP), and directed into two optical channels, Ch1 and Ch2, separated transversely by 1 cm. In the first experiment (Fig. 1b), two right-circularly polarized strong-control fields are resonant with the transition $|1\rangle \rightarrow |3\rangle$, and two left-circularly polarized weak-probe fields are nearly resonant with $|2\rangle \rightarrow |3\rangle$, but frequency shifted in opposite directions by the same one-photon detuning $|\Delta_0|$ using acousto-optical modulators (AOMs). To stabilize the phase relationship between the probe and control beams, all AOMs are driven by oscillators phase locked to each other. In each channel, the co-propagating probe and control fields set up the standard Λ-type EIT effect and create a long-lived ground-state coherence, with a lifetime of ~100 ms. The two spin waves are naturally coupled through the ballistic motion of ^{87}Rb atoms in the cell, where the randomness and irreversibility in the motion lays the foundation of the non-Hermiticity of the effective Hamiltonian.

The atom–light interaction in our driven system is described by the density-matrix formalism[48] (equations (4)–(17) in Methods). Under certain approximations, the following time-dependent non-Hermitian (Floquet) Hamiltonian $H_{\rm eff}$ is obtained to govern the dynamics of the two collective spin-wave excitations:

$$H_{\rm eff} = -\delta_B I + H, \text{ where } H = \begin{bmatrix} |\Delta_0| - i\gamma'_{12} & i\Gamma_c e^{-2i|\Delta_0|t} \\ i\Gamma_c e^{2i|\Delta_0|t} & -|\Delta_0| - i\gamma'_{12} \end{bmatrix} \quad (1)$$

Here, I is a 2×2 identity (or unit) matrix, $\gamma'_{12} = \gamma_{12} + \Gamma_c + 2\Gamma_p$, with γ_{12} the dephasing rate of the ground-state coherence, Γ_c the ground-state-coherence coupling rate between the two channels, and $2\Gamma_p = 2|\Omega_1|^2/\gamma_{31}$ the total pumping rate by the two control beams with the same Rabi frequency Ω_1, where γ_{31} is the atomic optical coherence decay rate. We note that the determinant of $H_{\rm eff}$, $\mathrm{Det}[H_{\rm eff}]$, is the denominator of the two coupled ground-state coherences $-[\gamma'_{12} + i(|\Delta_0| - \delta_B)][\gamma'_{12} + i(-|\Delta_0| - \delta_B)] + \Gamma_c^2$ (see equations (18) and (19) in Methods). The resonance condition of the coupled system is met when $\mathrm{Det}[H_{\rm eff}] = 0$, whose solutions, coinciding with the two eigenvalues of H, define the appearance of the two eigen-EIT supermodes (in terms of δ_B), with their real and imaginary parts being the line centres and linewidths, respectively. Experimentally, δ_B is a parameter that is swept to extract the eigenvalues of H. From another point of view, δ_B can be considered as a common offset to the diagonal elements of H; in turn, H can be mathematically produced from $H_{\rm eff}$ by choosing a different frequency reference, indicating that, without the $-\delta_B I$ term, H recovers the essential physics. As such, H will be our starting point throughout this work.

For simplicity, we consider the Hamiltonian H in equation (1) at periodically distributed discrete time points satisfying $e^{2i|\Delta_0|t} = 1$. This reduces H to a simpler form:

$$H' = \begin{bmatrix} |\Delta_0| - i\gamma'_{12} & i\Gamma_c \\ i\Gamma_c & -|\Delta_0| - i\gamma'_{12} \end{bmatrix} \quad (2)$$

with its eigenvalues corresponding to the two eigen-EIT supermodes

$$\omega_\pm = -i\gamma'_{12} \pm \sqrt{\Delta_0^2 - \Gamma_c^2} \quad (3)$$

Here, the real parts of $\omega_\pm$ are the values of δ_B which correspond to the resonance centres of the two coupled-EIT eigenmodes, and the imaginary parts represent their linewidths. As the essential results of this work, equations (1)–(3) contain rich physics and possess many interesting properties. First of all, for this 2×2 matrix, H satisfies $\hat{P}\hat{T}H = -H$ (that is, $\{H, \hat{P}\hat{T}\} = 0$) in contrast to $\hat{P}\hat{T}H = H$ (that is, $[H, \hat{P}\hat{T}] = 0$) for conventional PT symmetry; hence, we term H anti-PT-symmetric. In addition, this Hamiltonian leads to an intriguing phase transition exhibited on the two eigen-EIT spectral branches. Specifically, in the symmetry-unbroken regime ($|\Delta_0| < \Gamma_c$), the two eigen-EIT resonances coincide at the centre $\delta_B = 0$, but with different linewidths. The anti-PT symmetry breaking occurs at the exceptional point $|\Delta_0| = \Gamma_c$ where the two supermodes perfectly overlap. When $|\Delta_0| > \Gamma_c$, the driven system enters the symmetry-broken regime, and the resonances bifurcate and exhibit level anti-crossing, resembling a passively coupled system.

The spectral profiles of the two eigen-EIT spectra can be experimentally probed by slowly sweeping the magnetic field with time and measuring the weak-probe transmission. Therefore, the measured probe transmission is a function of both δ_B (lower x-axis) and time (upper x-axis), as shown in Fig. 2a1,a2 and b1,b2. As expected from equation (1), the EIT spectra display beating patterns

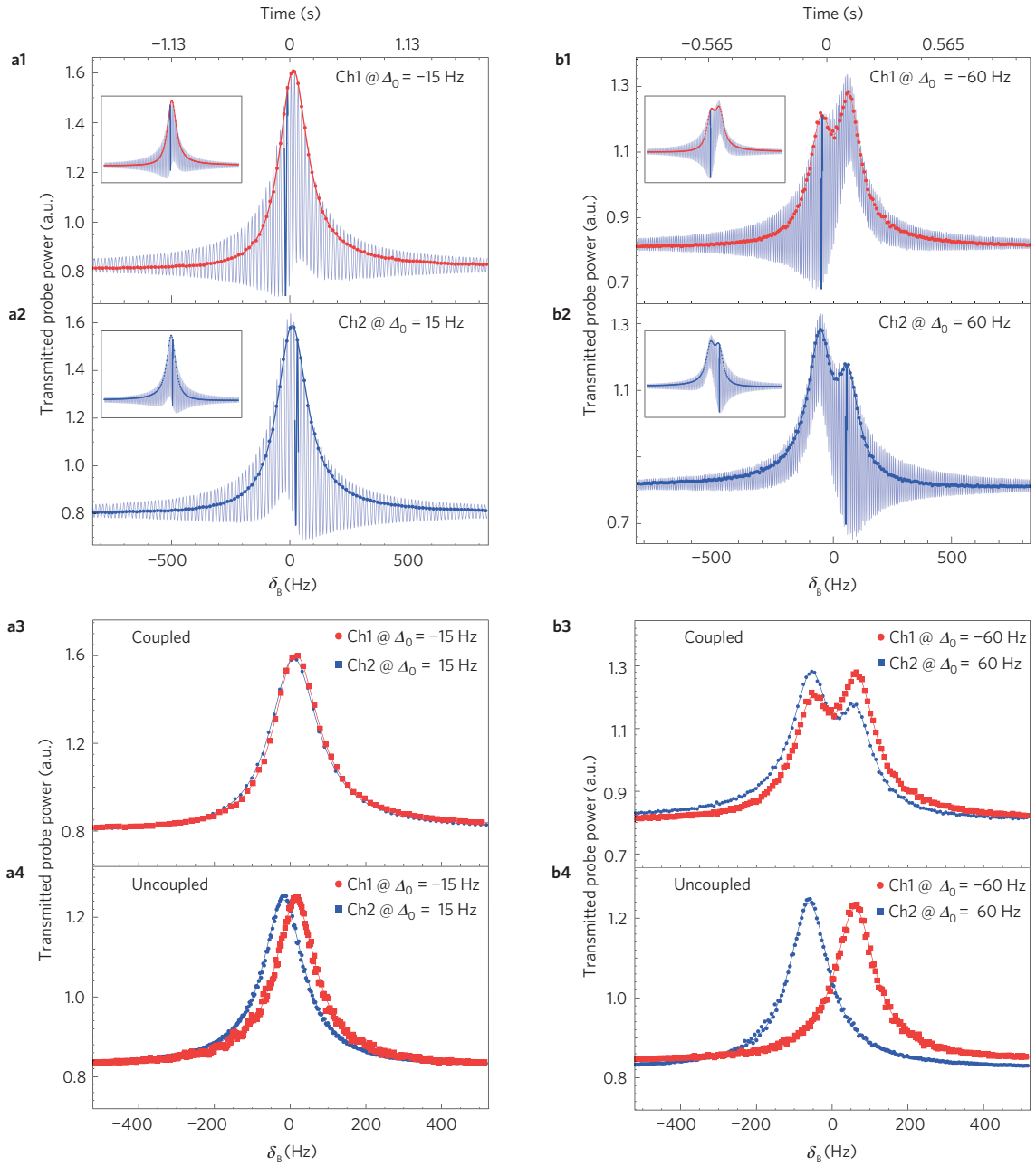

Figure 2 | Representative transmission spectra of output probe light in anti-PT symmetry. a1,**a2**, Typical transmission spectra of output probe light after Ch1 (with the probe red-detuned from the control by ∼15 Hz) and Ch2 (with the probe blue-detuned from the control by ∼15 Hz) in the regime of anti-PT unbroken phase, exhibiting a beating frequency of ∼30 Hz. **b1**,**b2**, Typical transmission spectra of output probe light with probe detuning ∓60 Hz in Ch1 and Ch2, respectively, in the regime of broken anti-PT phase. The bold, dotted curves in **a1**,**a2**,**b1**,**b2** are the EIT spectra extracted at time points t which satisfy $e^{i(2|\Delta_0|t+\Delta\varphi)}=1$, and the beating notes marked in dark blue are for the phase reference (Methods). The insets are calculated curves from the modified theory (Methods). **a3**,**b3**, Comparison of the dotted curves in Ch1 (**a1** and **b1**) and Ch2 (**a2** and **b2**) plotted together. **a4**,**b4**, Uncoupled EIT spectra separately measured from Ch1 (with red detuning ∼15 Hz/∼60 Hz) with both channels' control and only Ch1's probe input on, and from Ch2 (with blue detuning ∼15 Hz/∼60 Hz) with both channels' control and only Ch2's probe input on. The experimental parameters here are control powers of ∼180 μW and probe powers of ∼3.7 μW.

(light-blue curves in Fig. 2a1,a2 and b1,b2) oscillating at a frequency $|2\Delta_0|$. The physical origin of the beating can be understood as follows. The simultaneous presence of the oppositely detuned probes in Ch1 and Ch2 locally creates two spin waves within the laser-beam volumes that precess, respectively, with $e^{-i|\Delta_0|t}$ and $e^{i|\Delta_0|t}$ in a common rotating frame. Meanwhile, the atomic thermal motion, at a much faster timescale than that needed for steady-state coherence formation, redistributes and mixes the two spin waves coherently within the entire vapour cell. The total coherence in each channel is thus the sum of the two spin waves evolving at $e^{i|\Delta_0|t}$ and $e^{-i|\Delta_0|t}$. Consequently, its amplitude is modulated at frequency $|2\Delta_0|$, giving rise to beating in the probe transmission spectra. Figure 2 shows two sets of representative probe transmission spectra with $\Delta_0=\mp 15$ Hz (Fig. 2a1,a2) in the symmetry-unbroken regime and $\Delta_0=\mp 60$ Hz (Fig. 2b1,b2) in the symmetry-broken regime. From the beating spectra, one can extract a set of EIT spectra, as denoted by the red/blue dots, for a particular value of $e^{i(2|\Delta_0|t+\Delta\varphi)}$, where $\Delta\varphi$ is the difference between the two channels' input probe–control

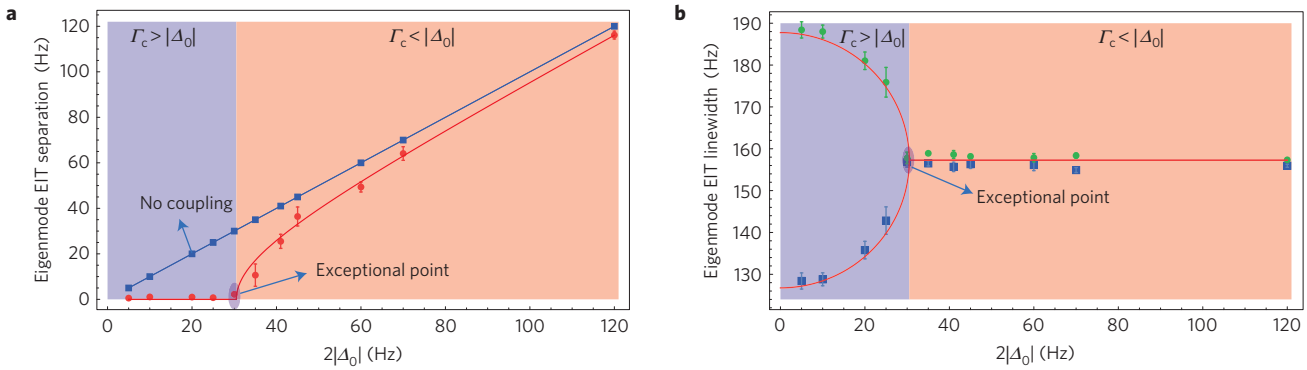

Figure 3 | Anti-PT supermodes in coupled-EIT channels in a homogeneous, warm ^{87}Rb vapour cell. a,b, Characteristics of the real part Re[ω] (**a**) and imaginary part Im[ω] (**b**) of the two eigenfrequencies of the coupled-EIT supermodes as a function of the probe detuning $|\Delta_0|$. The data points are obtained from curve fitting the measured transmission spectra to the theoretical result. In **a**, as a comparison, the blue squares represent the EIT peak separation between two uncoupled channels, and the red dots are for the coupled case with both Ch1 and Ch2 on. In **b**, the green dots and blue squares are the extracted linewidths of the two eigen-EIT modes, respectively. The error bars are standard deviations obtained from ten measurements. As described in the text, the linewidth values here are in good agreement with an independent check. The experimental parameters here are the same as those in Fig. 2.

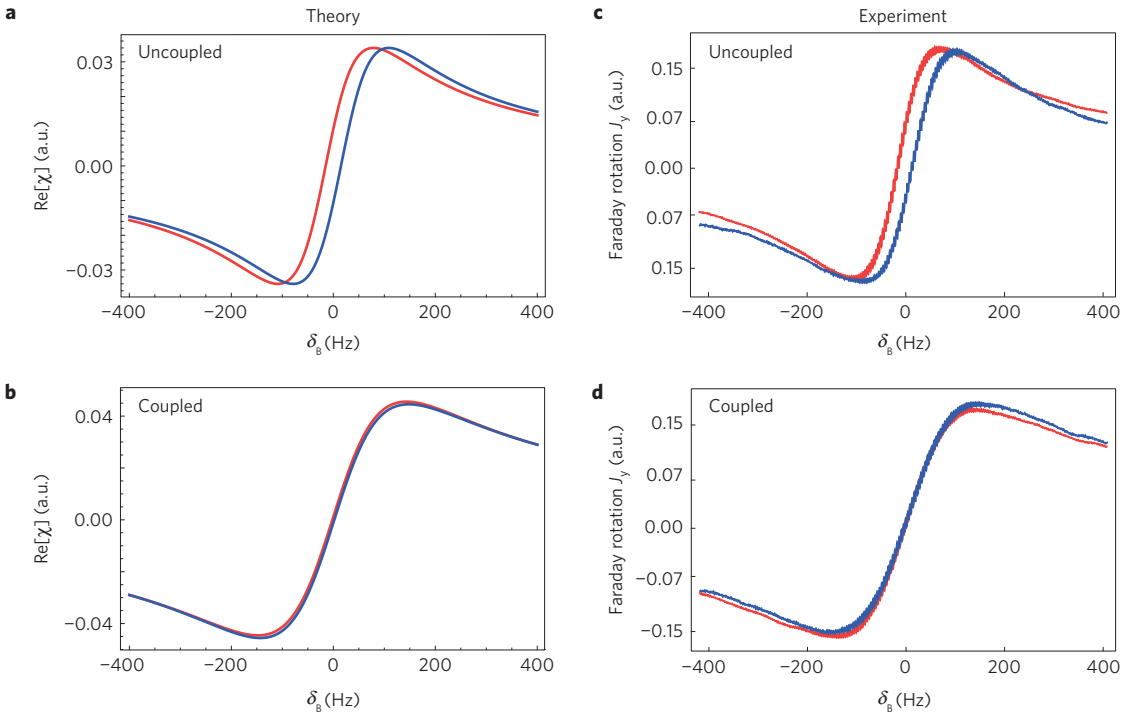

Figure 4 | Theoretical calculation and experimental demonstration of refractionless propagation of light ($n = 1 + \mathrm{Re}[\chi]/2 = 1$) assisted by anti-PT symmetry in the symmetry-unbroken regime. a,b, Theoretical results. In the presence of two magnetic fields (giving a change of Δ_B to the two-photon detuning) with opposite signs in Ch1 and Ch2, in the uncoupled case, with only the linearly polarized beam in one channel on, the left-circularly polarized component in Ch1 (blue) and that in Ch2 (red) experience nonzero Re[χ] at $\delta_B = 0$ (**a**). In contrast, when both channels are on, they see zero Re[χ] at $\delta_B = 0$ when the coupled system is operated in the symmetry-unbroken region (**b**). **c,d**, Experimental results. In the presence of two artificially created magnetic fields with opposite signs in Ch1 and Ch2, the linearly polarized light in Ch1 and Ch2 experiences nonzero and reversed Faraday rotations (proportional to Re[χ]) at $\delta_B = 0$, when only one channel's linearly polarized beam is on (uncoupled case) (**c**). When both the linearly polarized beams are on (coupled case), the rotation angle becomes zero at $\delta_B = 0$ for both channels, in good agreement with the theoretical prediction (**d**). The laser power for each linearly polarized light beam is 140 μW. The two circularly polarized off-resonant beams with opposite helicity in the two channels to create the fictitious magnetic field have powers of 150 μW, and are red-detuned from the $|F = 2\rangle \rightarrow |F' = 1\rangle$ transition by 1.3 GHz. The beam size for all lasers is approximately 1.2 mm in diameter and $\Delta_B = 15$ Hz.

relative phases (see Methods). The spectra are fitted (red/blue lines) by a weighted sum of the two eigen-EIT spectra (see equations (18) and (19) in Methods) to give the linewidth and line centre values as predicted by equation (3). As one can see, both the experimental EIT spectra with the beat and the extracted spectra show good agreement with the corresponding theoretical simulations (insets). For $\Delta_0 = \mp 15$ Hz, the two eigen-EIT spectra (Fig. 2a3) coalesce at $\delta_B = 0$, while for $\Delta_0 = \mp 60$ Hz, the two spectra (Fig. 2b3) are pulled closer to each other without complete overlap, compared to the uncoupled EIT spectra (Fig. 2a4 and b4) separately measured from Ch1/Ch2 with both control fields on but only Ch1's/Ch2's probe on.

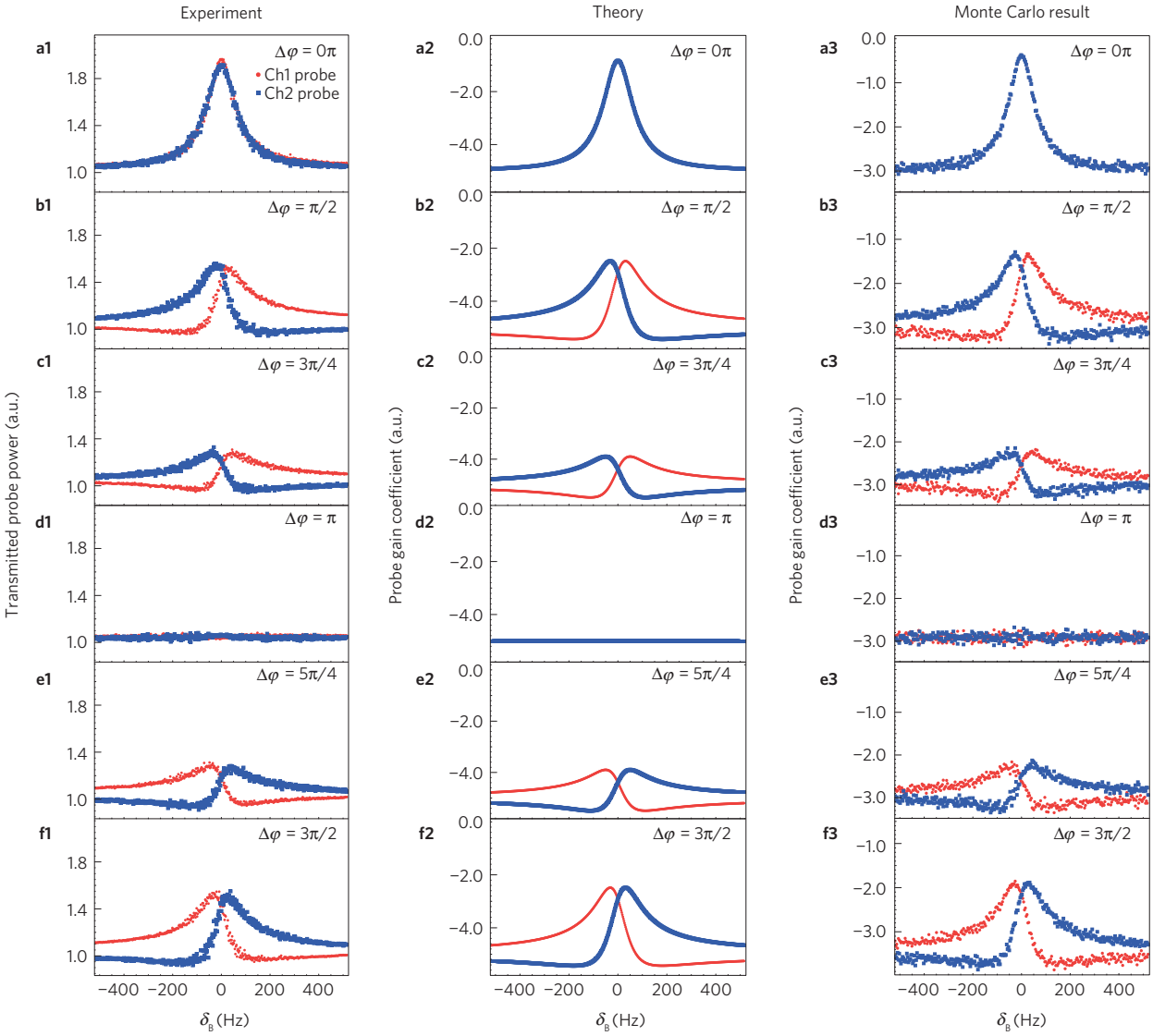

Figure 5 | Observation of interference between two EIT channels by manipulating the relative-phase difference among laser beams. For $|\Delta_0|=0$, when all the beams in both channels are on, the EIT spectra of the output probes are measured for different relative phases of the input optical fields, $\Delta\varphi=\Delta\varphi_1-\Delta\varphi_2$, where $\Delta\varphi_i$ is the probe–control relative phase in the ith channel. Depending on $\Delta\varphi$, the interference effect may change the EIT spectra dramatically. **a1**–**f1**, Experimental results, **a2**–**f2**, results calculated from the modified theory (see Methods), and **a3**–**f3**, Monte Carlo simulations (see Methods), for $\Delta\varphi=0,\pi/2,3\pi/4,\pi,5\pi/4,3\pi/2$. In **a2**–**f2** and **a3**–**f3** the plots are of the theoretical probe gain coefficients (negative value means absorption), proportional to the imaginary part of the probe's susceptibility. Experimental parameters: control powers of ~155 μW and probe powers of ~3.7 μW. Parameters used in the theoretical calculations: $\gamma_{12}=2\pi\times 7.5$ Hz, $\Gamma_c=2\pi\times 15$ Hz, $\gamma_{13}=2\pi\times 500$ MHz, $|\Omega_1^{(1,2)}|=2.4\times10^{-4}\gamma_{13}$, $|\Omega_2^{(1,2)}|=5\times10^{-5}\gamma_{13}$. Parameters used in the Monte Carlo simulations: $|\Omega_1^{(1,2)}|=2\pi\times 1.0$ MHz, $|\Omega_2^{(1,2)}|=0.1\times|\Omega_1^{(1,2)}|$, $\gamma_{13}=2\pi\times 500$ MHz, the attenuation factor of the ground-state coherence and population difference upon each wall collision is $e^{-(1/250)}$ (equivalent to $\gamma_{12}=2\pi\times 7.5$ Hz), the laser-beam size and cell size are set to be the same as the experimental values.

The evolution of the anti-PT supermodes is carefully examined by varying $|\Delta_0|$. By applying the method elaborated in Methods, the extracted line centres and their corresponding linewidths are plotted as a function of $|2\Delta_0|$ in Fig. 3, showing excellent agreement with theoretical predictions. Remarkably, the current system has high resolution of the phase-transition threshold at the Hz level. The experimental data (Fig. 3) evidently reveals the exceptional point occurring at $|2\Delta_0|=30.5$ Hz, which implies Γ_c of about 15 Hz. According to equation (3), when $\Delta_0=0$ the full linewidth difference between the two supermodes should be $4\Gamma_c$. This is verified from the fitting curve to the experimental data in Fig. 3b. Besides, equation (3) predicts the full linewidth of the lower eigenmode near $\Delta_0=0$ to be $2(2\Gamma_p+\gamma_{12})$. To confirm this prediction experimentally, we first allow only one channel on and obtain $\gamma_{12}=5$ Hz through the zero-power EIT linewidth measurement. By utilizing the full width of $2(\Gamma_p+\gamma_{12})=69$ Hz of the single-channel EIT spectrum (not shown), we deduce $2\Gamma_p=59$ Hz and $2(2\Gamma_p+\gamma_{12})=128$ Hz, which agrees with the width of the lower eigenmode for $\Delta_0=0$ shown in Fig. 3b. We note that Γ_c is mainly determined by experimental parameters such as the laser power and beam size, cell geometry, and atomic thermal velocity.

As illustrated above, in the regime of unbroken anti-PT symmetry, the initially separated EIT resonance centres of the two channels coalesce due to dissipative coupling. According to the Kramers–Kronig relation, this coalescence of spectra should result in zero Re[χ] (real part of the total linear susceptibility) at the overlapped EIT centre—that is, unit refractive index n

according to the relation $n = 1 + \mathrm{Re}[\chi]/2$ for an optically thin medium. Such refractionless (or unit-refraction) propagation of light is an exact analogue of the lossless propagation of light in a PT-symmetric system in its symmetry-unbroken regime, where probe powers coherently oscillate between two coupled subsystems without experiencing either gain or loss. To demonstrate the effect, we inject linearly x-polarized laser beams into both Ch1 and Ch2, resonant with the $5S_{1/2}|F=2\rangle \rightarrow 5P_{1/2}|F'=1\rangle$ transition, for which two circular polarization components form EIT. Instead of introducing $\pm|\Delta_0|$ to the two-photon detuning in two channels, we here produce opposite Zeeman shifts $\pm\Delta_B$ by effectively creating a local fictitious magnetic field through the a.c. Stark shifts of additional far-off-resonant circularly polarized lasers with opposite helicities in Ch1 and Ch2. At the output, for different δ_B we measure the transmitted intensity difference between the 45° and −45° polarization components (corresponding to the J_y component on the Poincaré sphere for light), which is the Faraday rotation signal and proportional to $\mathrm{Re}[\chi]$ for the left-circularly polarized component. When only one linearly polarized beam is on (uncoupled case), the curves of the Faraday rotation versus δ_B are slightly shifted in opposite directions, resulting in nonzero and opposite rotations at $\delta_B = 0$ in the two channels (Fig. 4c). In the coupled case with the linearly polarized beams in both channels on and $\Delta_B < \Gamma_c$, the atomic-coherence coupling now gives rise to zero Faraday rotation at $\delta_B = 0$ (Fig. 4d). The experimental result is in good agreement with the theoretical prediction (Fig. 4a,b).

Phase sensitivity arising from coherence transport is another intriguing feature of our system. We illustrate this for $\Delta_0 = 0$ (Fig. 1) when the ground-state coherences in the two channels share the same oscillation frequency. By tuning $\Delta\varphi = \Delta\varphi_1 - \Delta\varphi_2$, with $\Delta\varphi_1$ ($\Delta\varphi_2$) being the relative phase between the input control and probe in Ch1 (Ch2), nontrivial interference phenomena can occur between the two channels. Let us recall that, at steady state, the conventional Λ-type EIT system[36] is phase insensitive, since the probe transmission is independent of the relative phase between the input control and probe. Due to the coupling of the two spin waves, in contrast, the coupled-EIT system here becomes phase sensitive. As an example, Fig. 5 shows the output probe's EIT spectra of the two channels for various $\Delta\varphi$. Specifically, as $\Delta\varphi = \pi$, the EIT amplitudes (Fig. 5d1) are reduced to zero because of complete destructive interference between the two channels, in contrast to the maximal EIT amplitude for $\Delta\varphi = 0$ (Fig. 5a1). In the intervening region the dispersive feature appears (Fig. 5b1–c1 and e1–f1), generally associated with many phase-sensitive processes. The experimental data is confirmed both by our simplified analytical theory (Fig. 5a2–f2) and the Monte Carlo simulations (Fig. 5a3–f3, Methods), suggesting an agreement between the two theoretical approaches. The observation of such nonlocal interference implies that two spatially separated light beams can interfere with each other, contrary to conventional interference experiments, where the light beams must overlap.

The anti-PT system proposed here further provides a versatile way for photon–photon interactions. Despite the configuration of control/probe fields in Fig. 1b permitting linear interaction between the two weak-probe fields, this interaction can be modified to become nonlinear by choosing the pumping configuration depicted in Fig. 6a. Here, the effective Hamiltonian governing the ground-state-coherence coupling between two channels takes a similar form to equation (1) and remains anti-PT-symmetric, if the two-photon detunings in the two channels are properly set. Interestingly, the resulting nonlinear process is analogous to the well-known four-wave mixing (FWM)[49], and the two probes play similar roles to those of the Stokes and anti-Stokes fields in FWM. Intuitively, as the atomic coherence is being created in Ch1, the population is driven from $|1\rangle$ to $|2\rangle$; when this atom enters Ch2, the population is then brought back to $|1\rangle$. The process is continuously boosted along with the coherence transfer. As a result, both weak-probe fields are coherently amplified subject to the phase-matching condition. To confirm the analysis, we have carried out Monte Carlo simulations for the simple case of zero probe detunings. In Fig. 6b, the probe transmissions from both channels are plotted as a function of δ_B, assuming the initial phases of all optical fields to be zero. We find gain in both channels around $\delta_B = 0$. For large δ_B, although the phase-matching condition is still satisfied, the reduced ground-state coherence provides insufficient gain to compensate loss, which indicates that coherence plays an essential role in this FWM-like process. To further assess the nonlinear interaction, let us look at the probe transmissions for $\delta_B = 0$ by varying the phases $(\theta_{p1}, \theta_{p2})$ of the two probe fields. The simulation is presented in Fig. 6c, where two probe phases are swept together ($\theta_{p1} = \theta_{p2}$) whilst the two control phases (θ_c) are set at zero. Efficient FWM is expected to occur in our system when perfect phase matching is approached—that is, $\theta_{p1} + \theta_{p2} = 2\theta_c + 2m\pi$ with m an integer. Such an intuition is verified by the simulation shown in Fig. 6c, where the maximal gain indeed appears at $\theta_{p1,p2} = 0,\ \pi,\ 2\pi$. Complete theoretical modelling including nonzero probe detunings and the effects of the exceptional point will be considered in the future. To the best of our knowledge, so far all demonstrations of EIT-assisted nonlinear optics are based on optical nonlinearities inherent to suitable multilevel atomic structures[36]. In comparison, here the effective nonlinearity is built from coherence transport.

Given the tight connection of our system to magnetometers, slow light and quantum memory[50], new directions may be opened up for precision measurements, quantum optics and quantum information science. The EIT spectra with beating is similar to Ramsey fringes and can thus be used for precisely measuring the optical phase or the magnetic field. It is also intriguing to investigate the possibility of using the synthetic FWM configuration described above to entangle two spatially non-overlapping weak lasers, and to explore the effect of the phase transition in anti-PT symmetry on quantum noise. Furthermore, with some modifications this system can be switched to be PT-symmetric. Despite the mediator analysed in this work being freely moving atoms, similar strategies might be extended to other systems where the indirect coupling is established through, but not limited to, electrons, polaritons, plasmas, or phonons.

Methods

Methods, including statements of data availability and any associated accession codes and references, are available in the online version of this paper.

Received 25 September 2015; accepted 21 June 2016; published online 15 August 2016

References

1. Bender, C. M. & Boettcher, S. Real spectra in non-Hermitian Hamiltonians having PT symmetry. *Phys. Rev. Lett.* **80,** 5243–5246 (1998).
2. Bender, C. M., Boettcher, S. & Meisinger, P. N. PT-symmetric quantum mechanics. *J. Math. Phys.* **40,** 2201–2229 (1999).
3. Bender, C. M. Making sense of non-Hermitian Hamiltonians. *Rep. Prog. Phys.* **70,** 947–1018 (2007).
4. Mostafazadeh, A. Pseudo-Hermiticity versus PT symmetry: the necessary condition for the reality of the spectrum of a non-Hermitian Hamiltonian. *J. Math. Phys.* **43,** 205–214 (2002).
5. El-Ganainy, R., Makris, K. G., Christodoulides, D. N. & Musslimani, Z. H. Theory of coupled optical PT-symmetric structures. *Opt. Lett.* **32,** 2632–2634 (2007).
6. Guo, A. *et al*. Observation of PT-symmetry breaking in complex optical potentials. *Phys. Rev. Lett.* **103,** 093902 (2009).
7. Ruter, C. E. *et al*. Observation of parity–time symmetry in optics. *Nature Phys.* **6,** 192–195 (2010).
8. Bittner, S. *et al*. PT symmetry and spontaneous symmetry breaking in a microwave billiard. *Phys. Rev. Lett.* **108,** 024101 (2012).
9. Regensburger, A. *et al*. Parity–time synthetic photonic lattices. *Nature* **488,** 167–171 (2012).

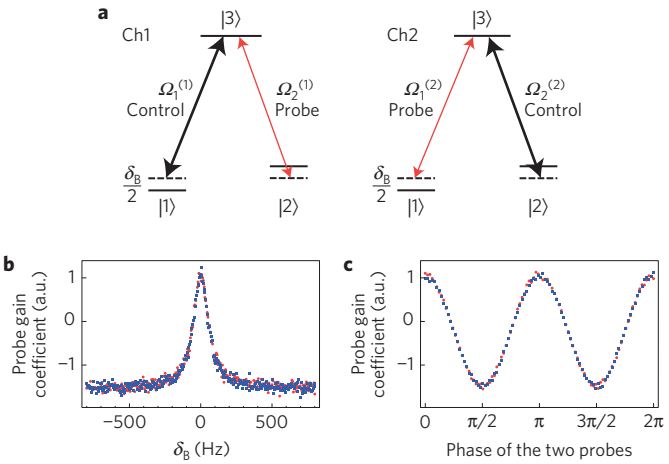

Figure 6 | Proposal for effective nonlinear interaction between two weak-probe fields aided by anti-PT-symmetric coupling of spin waves. **a**, Light configuration used to realize a four-wave-mixing-like process. Different from Fig. 1b, the two control (probe) fields in the two channels have opposite circular helicities, and are coupled to different transitions. To realize the anti-PT-symmetric Hamiltonian (equation (1)) for the coupled spin waves, the two probe frequency detunings (not drawn) should have the same sign, in contrast to that in Fig. 1b. The schematic in **a** is a special case with zero probe detuning Δ_0. **b**, Monte Carlo simulation of the two probe's gain coefficients, proportional to the imaginary part of the probe's susceptibility, as a function of δ_B. Here, positive (negative) values stand for gain (absorption). For simplicity, the initial phases of all laser fields are set to be zero. A maximal gain of 22% can be obtained in the current experimental conditions, and the linewidth of the gain curve here is determined by the overall decay rate γ'_{12} of the ground-state coherence, as described in equation (1). **c**, Monte Carlo simulation of two probe transmissions when the initial probe phases are synchronized and swept together, the initial phases of the two control fields are set at zero, and $\delta_B = 0$. The displayed phase sensitivity, originating from phase-matching condition, implies that the process is akin to a normal phase-sensitive FWM in nonlinear optics. Parameters used in the simulation: the Rabi frequencies of the two controls (probes) take the same values as those in the Monte Carlo simulation in Fig. 5. All other parameters are also the same.

10. Feng, L. *et al*. Experimental demonstration of a unidirectional reflectionless parity–time metamaterial at optical frequencies. *Nature Mater.* **12,** 108–113 (2013).
11. Sun, Y., Li, H.-q., Li, J. & Chen, H. Experimental demonstration of a coherent perfect absorber with PT phase transition. *Phys. Rev. Lett.* **112,** 143903 (2014).
12. Wimmer, M. *et al*. Observation of optical solitons in PT-symmetric lattices. *Nature Commun.* **6,** 7782 (2015).
13. Chang, L. *et al*. Parity–time symmetry and variable optical isolation in active-passive-coupled microresonantors. *Nature Photon.* **8,** 524–529 (2014).
14. Hodaei, H., Miri, M.-A., Heinrich, M., Christodoulides, D. N. & Khajavikhan, M. Parity–time-symmetric microring lasers. *Science* **346,** 975–978 (2014).
15. Makris, K. G., El-Ganainy, R., Christodoulides, D. N. & Musslimani, Z. H. Beam dynamics in PT symmetric optical lattices. *Phys. Rev. Lett.* **100,** 103904 (2008).
16. Lin, Z. *et al*. Unidirectional invisibility induced by PT-symmetric periodic structures. *Phys. Rev. Lett.* **106,** 213901 (2011).
17. Longhi, S. Invisibility in PT-symmetric complex crystals. *J. Phys. A* **44,** 485302 (2011).
18. Mostafazadeh, A. Invisibility and PT symmetry. *Phys. Rev. A* **87,** 485302 (2011).
19. Longhi, S. Bloch oscillations in complex crystals with PT symmetry. *Phys. Rev. Lett.* **103,** 123601 (2009).
20. Longhi, S. PT-symmetric laser absorber. *Phys. Rev. A* **82,** 031801(R) (2010).
21. Chong, Y. D., Ge, L. & Stone, A. D. PT-symmetry breaking and laser-absorber modes in optical scattering systems. *Phys. Rev. Lett.* **106,** 093902 (2011).
22. Nazari, F., Nazari, M. & Morawej-Farshi, M. K. A 2 × 2 spatial optical switch based on PT-symmetry. *Opt. Lett.* **36,** 4368–4370 (2011).
23. Sukhorukov, A. A., Xu, Z. Y. & Kivshar, Y. S. Nonlinear suppression of time reversals in PT-symmetric optical couplers. *Phys. Rev. A* **82,** 043818 (2010).
24. Miri, M., Wa, P. & Christodoulides, D. N. Large area single-mode parity–time-symmetric laser amplifiers. *Opt. Lett.* **37,** 764–766 (2012).
25. Benisty, H. *et al*. Implementation of PT symmetric devices using plasmonics: principle and applications. *Opt. Exp.* **19,** 18004–18019 (2011).
26. Bender, N. *et al*. Observation of asymmetric transport in structures with active nonlinearities. *Phys. Rev. Lett.* **110,** 234101 (2013).
27. Fleury, R., Sounas, D. & Alu, A. An invisible acoustic sensor based on parity–time symmetry. *Nature Commun.* **6,** 5905 (2015).
28. Berry, M. V. Optical lattices with PT symmetry are not transparent. *J. Phys. A* **41,** 244007 (2008).
29. Lü, X.-Y., Jing, H., Ma, J.-Y. & Wu, Y. PT-symmetry breaking chaos in optomechanics. *Phys. Rev. Lett.* **114,** 253601 (2015).
30. Ge, L. & Tureci, H. E. Antisymmetric PT-photonic structures with balanced positive-negative-index materials. *Phys. Rev. A* **88,** 053810 (2013).
31. Wu, J.-H., Artoni, M. & La Rocca, G. C. Parity–time-antisymmetric atomic lattices without gain. *Phys. Rev. A* **91,** 033811 (2015).
32. Hang, C., Huang, G. & Konotop, V. V. PT-symmetry with a system of three-level atoms. *Phys. Rev. Lett.* **110,** 083604 (2013).
33. Sheng, J., Miri, M.-A., Christodoulides, D. N. & Xiao, M. PT-symmetric optical potentials in a coherent atomic medium. *Phys. Rev. A* **88,** 041803(R) (2013).
34. Li, H., Dou, J. & Huang, G. PT symmetry via electromagnetically induced transparency. *Opt. Express* **21,** 32053–32062 (2013).
35. Harris, S. E. Electromagnetically induced transparency. *Phys. Today* **50 (7),** 36–42 (1997).
36. Fleischhauer, M., Imamoglu, A. & Marangos, J. P. Electromagnetically induced transparency: Optics in coherent media. *Rev. Mod. Phys.* **77,** 633–673 (2005).
37. Wen, J., Du, S., Chen, H. & Xiao, M. Electromagnetically induced Talbot effect. *Appl. Phys. Lett.* **98,** 081108 (2012).
38. Xiao, Y. *et al*. Slow light beam splitter. *Phys. Rev. Lett.* **101,** 043601 (2008).
39. Feng, L., Li, P., Jiang, L., Wen, J. & Xiao, Y. Coherence-assisted resonance with sub-transit-limited linewidth. *Phys. Rev. Lett.* **109,** 233006 (2012).
40. Ling, H., Li, Y. & Xiao, M. Electromagnetically induced grating: homogeneously broadened medium. *Phys. Rev. A* **57,** 1338–1344 (1998).
41. Liertzer, M. *et al*. Pump-induced exceptional points in lasers. *Phys. Rev. Lett.* **108,** 173901 (2012).
42. Ramezni, H., Kottos, T., Kovanis, V. & Christodoulides, D. N. Exceptional-point dynamics in photonic honeycomb lattices with PT symmetry. *Phys. Rev. A* **85,** 013818 (2012).
43. Cao, H. & Wiersig, J. Dielectric microcavities: Model systems for wave chaos and non-Hermitian physics. *Rev. Mod. Phys.* **87,** 61–111 (2015).
44. Rotter, I. A non-Hermitian Hamiltonian operator and the physics of open quantum systems. *J. Phys. A* **42,** 153001 (2009).
45. Moiseyev, N. *Non-Hermitian Quantum Mechanics* (Cambridge Univ. Press, 2011).
46. Rotter, I. & Bird, J. P. A review of progress in the physics of open quantum systems: theory and experiment. *Rep. Prog. Phys.* **78,** 114001 (2015).
47. Robinson, H. G., Ensberg, E. S. & Dehmelt, H. G. Preservation of a spin state in free atom inert surface collisions. *Bull. Am. Phys. Soc.* **3,** 9 (1958).
48. Scully, M. O. & Zubairy, M. S. *Quantum Optics* (Cambridge Univ. Press, 1997).
49. Boyd, R. W. *Nonlinear Optics* (Academic, 2008).
50. Novikova, I., Walsworth, R. & Xiao, Y. Electromagnetically induced transparency-based slow and stored light in warm atoms. *Laser Photon. Rev.* **6,** 333–353 (2012).

Acknowledgements

We are grateful to V. V. Albert for reading the manuscript. This work is supported by National Key Research Program of China under Grant No. 2016YFA0302000, and NNSFC under Grant No. 11322436. J.W. and L.J. acknowledge funding support from the ARO, the AFSOR MURI, the ARL CDQI program, the Alfred P. Sloan Foundation, and the David and Lucile Packard Foundation.

Author contributions

J.W., L.J. and Y.X. conceived the idea. Y.X. supervised the project. P.P. performed the experiment. W.C., P.P. and L.J. did the theoretical derivation and numerical calculations with contributions from all other authors. J.W., L.J. and Y.X. wrote the manuscript with contributions from all other authors. All contributed to the discussion of the project and analysis of the experimental data.

Additional information

Supplementary information is available in the online version of the paper. Reprints and permissions information is available online at www.nature.com/reprints. Correspondence and requests for materials should be addressed to J.W., L.J. or Y.X.

Competing financial interests

The authors declare no competing financial interests.

Methods

Derivation of the anti-PT-symmetric Hamiltonian. The system of interest is schematically depicted in Fig. 1a, where two optical channels 1 and 2 with no spatial overlap are each composed of a collinear weak-probe field and a strong-control field. The atomic level structure is the three-level Λ-type EIT configuration shown in Fig. 1b. Two identical, right-circularly polarized control fields with the same Rabi ($\Omega_1^{(1)}=\Omega_1^{(2)}$) and angular ($\omega_1^{(1)}=\omega_1^{(2)}$) frequencies are applied on resonance with the atomic transition $|1\rangle\rightarrow|3\rangle$; while two left-circularly polarized probe fields (with $\Omega_2^{(1)}=\Omega_2^{(2)}$ and $\omega_2^{(1)}\neq\omega_2^{(2)}$) are tuned almost resonant with the transition $|2\rangle\rightarrow|3\rangle$, but frequency shifted in opposite directions by a small value $|\Delta_0|$. Under the EIT conditions, the population is mainly distributed in $|2\rangle$. A common magnetic field is applied to implement the two-photon detuning in the EIT spectra measurement. The two-photon detunings in Ch1 and Ch2 are $\delta^{(1)}=\Delta_1^{(1)}-\Delta_2^{(1)}=|\Delta_0|-\delta_B$ and $\delta^{(2)}=\Delta_1^{(2)}-\Delta_2^{(2)}=-|\Delta_0|-\delta_B$, respectively, where $\Delta_1^{(j)}$ ($\Delta_2^{(j)}$) is the one-photon detuning of the control (probe) in the jth channel ($j=1,2$). The ground-state coherences in the two channels are effectively coupled through thermal motion at a rate Γ_c.

Under the rotating-wave approximation, the atom–light interaction can be described by the following density-matrix formalism[48],

$$\begin{cases}
\dot{\rho}_{11}^{(1)}=-i\Omega_1^{(1)}\rho_{13}^{(1)}+i\Omega_1^{(1)*}\rho_{31}^{(1)}+\gamma\rho_{33}^{(1)}-\gamma'\left(\rho_{11}^{(1)}-\rho_{22}^{(1)}\right) & (4)\\
\dot{\rho}_{22}^{(1)}=-i\Omega_2^{(1)}\rho_{23}^{(1)}+i\Omega_2^{(1)*}\rho_{32}^{(1)}+\gamma\rho_{33}^{(1)}+\gamma'\left(\rho_{11}^{(1)}-\rho_{22}^{(1)}\right) & (5)\\
\dot{\rho}_{31}^{(1)}=-\left(\gamma_{13}-i\Delta_1^{(1)}\right)\rho_{31}^{(1)}+i\Omega_2^{(1)}\rho_{21}^{(1)}+i\Omega_1^{(1)}\left(\rho_{11}^{(1)}-\rho_{33}^{(1)}\right) & (6)\\
\dot{\rho}_{32}^{(1)}=-\left(\gamma_{23}-i\Delta_2^{(1)}\right)\rho_{32}^{(1)}+i\Omega_1^{(1)}\rho_{12}^{(1)}+i\Omega_2^{(1)}\left(\rho_{22}^{(1)}-\rho_{33}^{(1)}\right) & (7)\\
\dot{\rho}_{11}^{(2)}=-i\Omega_1^{(2)}\rho_{13}^{(2)}+i\Omega_1^{(2)*}\rho_{31}^{(2)}+\gamma\rho_{33}^{(2)}-\gamma'\left(\rho_{11}^{(2)}-\rho_{22}^{(2)}\right) & (8)\\
\dot{\rho}_{22}^{(2)}=-i\Omega_2^{(2)}\rho_{23}^{(2)}+i\Omega_2^{(2)*}\rho_{32}^{(2)}+\gamma\rho_{33}^{(2)}+\gamma'\left(\rho_{11}^{(2)}-\rho_{22}^{(2)}\right) & (9)\\
\dot{\rho}_{31}^{(2)}=-\left(\gamma_{13}-i\Delta_1^{(2)}\right)\rho_{31}^{(2)}+i\Omega_2^{(2)}\rho_{21}^{(2)}+i\Omega_1^{(2)}\left(\rho_{11}^{(2)}-\rho_{33}^{(2)}\right) & (10)\\
\dot{\rho}_{32}^{(2)}=-\left(\gamma_{23}-i\Delta_2^{(2)}\right)\rho_{32}^{(2)}+i\Omega_1^{(2)}\rho_{12}^{(2)}+i\Omega_2^{(2)}\left(\rho_{22}^{(2)}-\rho_{33}^{(2)}\right) & (11)\\
\dot{\rho}_{12}^{(1)}=-\left(\gamma_{12}+i\delta^{(1)}\right)\rho_{12}^{(1)}+i\Omega_1^{(1)*}\rho_{32}^{(1)}-i\Omega_2^{(1)}\rho_{13}^{(1)} & \\
\quad-\left(\Gamma_c+\Gamma_p^{(2)}\right)\rho_{12}^{(1)}+\Gamma_c e^{-i2|\Delta_0|t}\rho_{12}^{(2)} & (12)\\
\dot{\rho}_{12}^{(2)}=-\left(\gamma_{12}+i\delta^{(2)}\right)\rho_{12}^{(2)}+i\Omega_1^{(2)*}\rho_{32}^{(2)}-i\Omega_2^{(2)}\rho_{13}^{(2)} & \\
\quad-\left(\Gamma_c+\Gamma_p^{(1)}\right)\rho_{12}^{(2)}+\Gamma_c e^{i2|\Delta_0|t}\rho_{12}^{(1)} & (13)\\
\rho_{11}^{(1)}(0)+\rho_{22}^{(1)}(0)+\rho_{33}^{(1)}(0)=1 & (14)\\
\rho_{11}^{(2)}(0)+\rho_{22}^{(2)}(0)+\rho_{33}^{(2)}(0)=1 & (15)
\end{cases}$$

Here, γ_{ij} represents the decay rate of the coherence between states $|i\rangle$ and $|j\rangle$, γ' stands for the decay rate of the ground-state population difference, γ is the decay rate of the excited state, and $\Gamma_p^{(j)}=(|\Omega_1^{(j)}|^2/\gamma_{23})$ denotes the optical pumping rate for EIT in the jth channel.

Since the optical coherences $\rho_{31}^{(j)}$ and $\rho_{32}^{(j)}$ decay much faster than the ground-state coherences $\rho_{12}^{(j)}$, we can assume that they follow the slow oscillations in the ground-state coherences. Therefore, by setting the time derivatives of optical coherences in equations (6) and (7) and (10) and (11) to be zero, one can express the optical coherences in terms of ground-state coherences. The control beams in the experiment are relatively weak such that the excited-state population $\rho_{33}^{(j)}=0$. Also, we assume that $\Omega_1^{(j)}\gg\Omega_2^{(j)}$, so that $\rho_{22}^{(j)}=1$. By adopting a procedure similar to that implemented in ref. 48, only equations (12) and (13) survive and play an essential role for describing the underlying physics. Thus, one can obtain the following coupled equations of two collective spin-wave excitations (or in short, spin waves) associated with the ground-state coherences, $\rho_{12}^{(1)}$ and $\rho_{12}^{(2)}$:

$$\begin{cases}
\dot{\rho}_{12}^{(1)}=-\left(\gamma'_{12}+i\delta^{(1)}\right)\rho_{12}^{(1)}+\Gamma_c e^{-2i|\Delta_0|t}\rho_{12}^{(2)}-\dfrac{\Omega_1^{(1)*}\Omega_2^{(1)}}{\gamma_{23}} & (16)\\
\dot{\rho}_{12}^{(2)}=-\left(\gamma'_{12}+i\delta^{(2)}\right)\rho_{12}^{(2)}+\Gamma_c e^{2i|\Delta_0|t}\rho_{12}^{(1)}-\dfrac{\Omega_1^{(2)*}\Omega_2^{(2)}}{\gamma_{23}} & (17)
\end{cases}$$

Here, $\gamma'_{12}=\gamma_{12}+\Gamma_c+\Gamma_p^{(1)}+\Gamma_p^{(2)}=\gamma_{12}+\Gamma_c+2\Gamma_p$ represents the total effective decay rate of the spin waves, with the assumption of equal control powers in Ch1 and Ch2. Information about the collective spin-wave excitations can be simply detected via EIT by measuring the weak-probe outputs after the cell, as their transmittances are linear functions of the ground-state coherence in the optically thin regime—that is, $\rho_{32}=(i\Omega_2+i\Omega_1\rho_{12})/\gamma_{23}$.

From the coupled equations (16) and (17), the effective non-Hermitian Hamiltonian $H_{\rm eff}$ (as shown in equation (1)) can be deduced that governs the dynamics of the two collective spin-wave excitations:

$$H_{\rm eff}=-\delta_B\mathbf{I}+H,\ \text{where}\ H=\begin{bmatrix}|\Delta_0|-i\gamma'_{12} & i\Gamma_c e^{-2i|\Delta_0|t}\\ i\Gamma_c e^{2i|\Delta_0|t} & -|\Delta_0|-i\gamma'_{12}\end{bmatrix}$$

It is straightforward to show H is anti-PT-symmetric because it satisfies $\hat{P}\hat{T}H=-H$, in contrast to $\hat{P}\hat{T}H=H$ in conventional PT symmetry. Another important feature of this equation is that H is symmetric under discrete time translations, $t\rightarrow t+\pi/|\Delta_0|$, and is hence a periodic function in time, $H(t)=H(t+\pi/|\Delta_0|)$ with the period $\pi/|\Delta_0|$ of the perturbation. Such an observation of the symmetry of the Hamiltonian (1) enables the use of the Floquet formalism, and could become another control in investigating the dynamics of the coupled spin waves.

In the adiabatic limit, the atomic dynamics follows the effective Hamiltonian (1), which evolves slowly under the presence of the terms $e^{\pm2i|\Delta_0|t}$. In the steady-state approximation, the two collective spin-wave excitations take the form

$$\begin{cases}
\rho_{12}^{(1)}=\dfrac{-\frac{\Omega_1^{(1)*}\Omega_2^{(1)}}{\gamma_{23}}\left(\gamma'_{12}+i\delta^{(2)}\right)-\frac{\Omega_1^{(2)*}\Omega_2^{(2)}}{\gamma_{23}}\Gamma_c e^{-2i|\Delta_0|t}}{\left(\gamma'_{12}+i\delta^{(1)}\right)\left(\gamma'_{12}+i\delta^{(2)}\right)-\Gamma_c^2} & (18)\\
\rho_{12}^{(2)}=\dfrac{-\frac{\Omega_1^{(2)*}\Omega_2^{(2)}}{\gamma_{23}}\left(\gamma'_{12}+i\delta^{(1)}\right)-\frac{\Omega_1^{(1)*}\Omega_2^{(1)}}{\gamma_{23}}\Gamma_c e^{2i|\Delta_0|t}}{\left(\gamma'_{12}+i\delta^{(1)}\right)\left(\gamma'_{12}+i\delta^{(2)}\right)-\Gamma_c^2} & (19)
\end{cases}$$

The physics behind equations (18) and (19) is the following. Each spin-wave excitation is a linear superposition of the two coupled-EIT eigenmodes, whose spectral profiles can be obtained by setting the denominator of equations (18) or (19) to zero. Each eigenmode has contributions from both channels and exhibits a beating frequency of $2|\Delta_0|$.

Equations (16) and (17) can be also perturbatively solved in the non-adiabatic limit. In such a case, in fact, one can expand the two spin-wave excitations in terms of Fourier series—that is, $\rho_{12}^{(1)}=\sum_{n=-\infty}^{n=\infty}\rho_{12}^{(1)}(n)e^{2in|\Delta_0|t}$ and $\rho_{12}^{(2)}=\sum_{n=-\infty}^{n=\infty}\rho_{12}^{(2)}(n)e^{2in|\Delta_0|t}$. Equations (12) and (13) can then be evaluated by matching terms with the same order. For the range of parameters in the current work, even truncating the series up to the first order $n=1$ would yield a good agreement between theory and experiment. After lengthy algebra, one can obtain:

$$\begin{cases}
\rho_{12}^{(1)}=\rho_{12}^{(1)}(0)+\rho_{12}^{(1)}(-2|\Delta_0|)e^{-i2|\Delta_0|t} & \\
\quad=\dfrac{1}{\gamma_{23}}\left(\dfrac{\Omega_1^{(1)*}\Omega_2^{(1)}(\gamma'_{12}+i\delta^{(1)})}{\Gamma_c^2-(\gamma'_{12}+i\delta^{(1)})^2}+\dfrac{\Gamma_c\Omega_1^{(2)*}\Omega_2^{(2)}}{\Gamma_c^2-(\gamma'_{12}+i\delta^{(2)})^2}e^{-i2|\Delta_0|t}\right) & (20)\\
\rho_{12}^{(2)}=\rho_{12}^{(2)}(0)+\rho_{12}^{(2)}(2|\Delta_0|)e^{i2|\Delta_0|t} & \\
\quad=\dfrac{1}{\gamma_{23}}\left(\dfrac{\Omega_1^{(2)*}\Omega_2^{(2)}(\gamma'_{12}+i\delta^{(2)})}{\Gamma_c^2-(\gamma'_{12}+i\delta^{(2)})^2}+\dfrac{\Gamma_c\Omega_1^{(1)*}\Omega_2^{(1)}}{\Gamma_c^2-(\gamma'_{12}+i\delta^{(1)})^2}e^{i2|\Delta_0|t}\right) & (21)
\end{cases}$$

We have proved that equations (20) and (21) can be converted back to equations (18) and (19) when the adiabatic condition is met. Our experiment was carried out in the adiabatic regime where Δ_0 and Γ_c are much smaller than γ'_{12}.

Criteria for phase reference selection. As can be seen from equations (18) and (19), to extract the linewidth and line centre of the eigen-EIT spectra from the measured EIT spectra containing beat patterns, we need to identify all the points on the beat with time t which give a fixed value to $e^{i(2|\Delta_0|t+\Delta\varphi)}$, where $\Delta\varphi$ is the difference between the two channels' input probe–control relative phases. For convenience, we choose time points satisfying $e^{i(2|\Delta_0|t+\Delta\varphi)}=1$. To identify these points, a reference point is needed such that all other points can be found at time intervals that are integral multiples of the beating period from it.

Equations (20) shows that, for Ch1, the d.c. part of the spin wave has its centre determined by the two-photon detuning of Ch1, while the centre of its a.c. part is determined by the two-photon detuning of Ch2. For the spin wave in Ch2 it is vice versa. Moreover, equation (20) implies that, for the Ch1 EIT spectra, only when $\delta_B=-|\Delta_0|$ (that is, $\delta^{(2)}=0$) do the atoms not impose an additional dynamical phase on top of the beating term $e^{-2i|\Delta_0|t}$. We note that the beat note at this location has the maximal amplitude across the whole spectral profile. Meanwhile, by examining the corresponding optical coherence for Ch1's probe field, we can see that, at the peak of the maximal beating note, $e^{-i(2|\Delta_0|t+\Delta\varphi)}=1$ on the time axis is satisfied. Similarly, equation (21) indicates that, for Ch2, such a beat note is located at $\delta_B=|\Delta_0|$. Based upon this analysis, in the experiment we first identify the beat note with the maximal amplitude and then choose its peak location as the time reference origin (see Fig. 2a1,a2 and b1,b2).

The phase criteria we used here are not the only possible choice, but a convenient one. In fact, if the reference origin is offset from the peak of the

maximal beat note, the lineshape of the extracted coupled-EIT spectra would be modified in some way. For our experimental conditions, for instance, in the regime where $\Gamma_c > |\Delta_0|$, the degree of tilting in the lineshape of EIT will change, due to the changed weight of the dispersive components; in the regime where $\Gamma_c < |\Delta_0|$, two equally weighted peaks in the extracted EIT spectra become unequal. Fortunately, such a situation does not affect the extracted values of the line centre and linewidth of the EIT eignemodes, but affects only the weights of the two eigenmodes and the ratio between the Lorentzian and dispersive components. The unequal peaks (red/blue curves in Fig. 2b1,b2) and slightly tilted Lorentzians (red/blue curves in Fig. 2a1,a2) indicate that the criteria stated above give a small deviation of the phase reference origin selected from the ideal value. This is mainly due to the finite number of beats available in the experiment as well as the small drift of input laser phases, $\Delta\varphi$. For example, in the spectra from Ch1, the beat with the maximal amplitude is not precisely located at $\delta_B = -|\Delta_0|$. Such a small discrepancy is unavoidable and vanishes only for infinitely dense beat notes, which require an infinitely long data acquisition time and absolutely no phase instability in any of the optical fields.

Modification of the model. Although the theory described above, named 'unmodified theory' from now on, captures the essential physics behind the observed anti-PT symmetry, a careful comparison of the experimentally measured EIT spectra still reveals a discrepancy with respect to those computed from the unmodified theory. An example (shown in Supplementary Fig. 1) exhibits a disagreement between the unmodified theory (Supplementary Fig. 1 a2–d2) and the experiment (Supplementary Fig. 1 a1–d1). In particular, the calculated beating contrast is much smaller than that measured experimentally. In addition, for the case of $\Delta_0 = 0$, EIT spectra computed (not shown) from equations (18) and (19) do not agree with the complete destructive interference effect observed for $\Delta\varphi = \pi$ in the experiment (Fig. 5d1). This discrepancy occurs because we neglected coherence transfer between the cell regions inside and outside the laser beams; in other words, the full role of motional averaging in the system was not taken into account. In practice, atoms fly into and out of the laser beams rapidly and, as a consequence, coherences produced from the two channels mix much better within the whole cell volume than those described from the simple model presented above. Intuitively, this fast mixing should result in a higher beat contrast for $\Delta_0 \neq 0$ and a better cancellation of EIT at $\Delta\varphi = \pi$ for $\Delta_0 = 0$.

Before addressing this issue, let us recall that the EIT lineshape in a buffer-gas or wall-coated vapour cell has a dual structure if the laser-beam size is much smaller than the cell volume[38,51–54]. The broad spectral structure comes from the one-time interaction of the atoms and the light, with a linewidth determined by the transit time across the laser beam (~300 kHz in our experiment). The narrower structure on top, due to the much longer time that the atoms spend outside the laser beam experiencing dark evolution, has a linewidth (~100 Hz in our experiment) determined by the ground-state-coherence decay rate and the optical pumping rate. Given the large difference in the two linewidths, the broad structure may be considered as a constant offset added to the coherence calculated by the simple model (equations (16) and (17)) in the frequency range of the narrow structure.

On the basis of the above analysis, we phenomenologically add an offset to the ground-state coherence to include the process of coherence exchange between the volumes inside and outside the laser beams. That is, we modify the source terms for the coherences in equations (16) and (17) as follows:

$$\begin{cases} \dot{\rho}_{12}^{(1)} = -\left(\gamma_{12}' + i\delta^{(1)}\right)\rho_{12}^{(1)} + \Gamma_c e^{-2i|\Delta_0|t}\rho_{12}^{(2)} - \dfrac{\Omega_1^{(1)*}\Omega_2^{(1)}}{\gamma_{23}}\left(\eta + \eta\dfrac{\gamma_{12}' + i\delta^{(1)}}{\Gamma_c}\right) & (22) \\ \dot{\rho}_{12}^{(2)} = -\left(\gamma_{12}' + i\delta^{(2)}\right)\rho_{12}^{(2)} + \Gamma_c e^{2i|\Delta_0|t}\rho_{12}^{(1)} - \dfrac{\Omega_1^{(2)*}\Omega_2^{(2)}}{\gamma_{23}}\left(\eta + \eta\dfrac{\gamma_{12}' + i\delta^{(2)}}{\Gamma_c}\right) & (23) \end{cases}$$

Here, the $((\gamma_{12}' + i\delta^{(1,2)})/\Gamma_c)$ terms on the right-hand side give rise to an offset of $\eta((\Omega_1^{(1,2)*}\Omega_2^{(1,2)})/\gamma_{23}\Gamma_c)$ to the coherences $\rho_{12}^{(1,2)}$ for the single-channel case (that is, setting the coherence of the other channel $\rho_{12}^{(2,1)}$ to be zero). Alternatively, this term can be understood as an additional source for $\rho_{12}^{(1,2)}$ contributed by the region outside the laser beams through coherence transport. The dimensionless constant η is a fitting parameter. It is evident that this modification does not change the effective Hamiltonian (1) of the system, because it affects only the source term for the coherence. Interestingly, such a simple correction made in the model enables a quantitative comparison with experimental data.

Equations (22) and (23) can be solved using the perturbative approach described above. The calculated EIT transmission spectra of the probe beams in the two channels are shown in Supplementary Fig. 1 a3–d3, which show an excellent agreement with the experimental measurements displayed in Supplementary Fig. 1 a1–d1. When plotting the EIT spectra with no beat, the phase reference origin here has been shifted by 1/30th of the beating period with respect to the above criteria, to match the shape of the EIT curve extracted from the experimental data (Fig. 2). In the calculations, we allow the magnetic field to vary slowly enough with time, as the sweeping magnetic field does in the experiment. The time t and δ_B are depicted, respectively, on the upper and lower horizontal axes. We also verified that the modified model shows an excellent agreement with the EIT interference experiment (Fig. 5a2–f2).

Monte Carlo simulations. To further verify the correctness of our theoretical model described above, we have carried out full Monte Carlo simulations. Previously, analytical models and two-dimensional Monte Carlo simulations have been developed to study repetitive atom–light interactions under EIT in both coated cells and buffer-gas cells, for a single-channel laser-beam geometry[51–54]. We here extend the Monte Carlo simulation to the current two-channel scenario. In the simulation, for simplicity, a round area is assumed to represent the laser-beam cross section. The atoms are allowed to move freely and collide with the cell wall, and the angular distribution relative to the surface normal of bounced atoms follows a cosine distribution[55]. For each time that the atom bounces off the cell wall, to account for the ground-state population difference and coherence decay, we assign an attenuation factor to the population difference and the ground-state coherence, and then let the atomic dynamics continue until the system reaches its steady state. Typically, 5,000 trajectories are averaged to reduce the heavy computational load of the simulation. An example (Fig. 5a3–f3) is provided for the case where $\Delta_0 = 0$. As we can see, the simulation matches the experiment very well.

Measurements and methods for curve fitting. As described above, the coupled-EIT eigenspectra measured by the probe transmittance exhibit an oscillatory pattern at a beating frequency of $2|\Delta_0|$. Experimentally, to properly acquire such a beating spectrum, the following conditions should be satisfied. First, the magnetic field is swept slowly enough such that the atoms form steady-state beat oscillations for each δ_B. Second, to prevent the beating from being washed out during time averaging over several magnetic-field-sweeping periods, the magnetic-field-sweeping period is maintained at integer multiples of the beating period. Third, $\Delta\varphi$ should not drift during each sweeping, otherwise the phase fluctuations may wash out the beating fringes during averaging. Therefore, after each scan, we recheck and make sure that $\Delta\varphi$ remains unchanged.

After acquiring the EIT spectra with the beat note, we locate the beat with the maximal amplitude (the bold dark-blue lines highlighted in Fig. 2a1,a2 and b1,b2), and set the position of this beat's peak as the time reference origin. Starting from this reference origin, the remaining discrete time points (red/blue dots in Fig. 2a1,a2 and b1,b2) are then sequentially identified at distances of integral multiples of the beating period. As the phase of the beat depends on the relative phase between the two coherences (oscillating at $e^{\pm i|\Delta_0|t}$ respectively) as well as δ_B (see equations (20)–(21)), these identified time points (red/blue dots) are located at different positions of the beat notes. The EIT spectra formed by these red/blue dots are a weighted sum of the two eigen-EIT supermodes as given in equation (3), whose linewidth and line centre can be then obtained by curve fitting. Note that the EIT spectra of either channel is sufficient to extract the line centres and linewidths of both eigenmodes, and each eigenmode is generally a tilted Lorentzian because it is composed of a Lorentzian and a dispersive component with the same linewidth and line centre, according to equations (18) and (19).

The two-channel EIT under coupling has a profile distinct from that without coupling. In our definition, the uncoupled EIT spectra from Ch1 (Ch2) are measured with both channels' control fields and only Ch1's (Ch2's) input probe on (see Fig. 2a4 and b4). In the experiment, we first turn on the control and probe fields in only one channel and optimize the laser frequencies to ensure a symmetric EIT lineshape. The coupled EIT is measured when the probe and control in both channels are on. The separation between the two uncoupled EIT resonance centres is simply $|2\Delta_0|$. When both channels are on, the extracted EIT spectral profiles deviate from a single Lorentzian. Here, on the one hand, due to a small phase offset as explained above, the existence of a small dispersive component slightly tilts the Lorentzian in the regime where $\Gamma_c > |\Delta_0|$. As a result, the extracted EIT spectrum in either channel is asymmetric with respect to δ_B. On the other hand, the lineshape in the regime where $\Gamma_c < |\Delta_0|$ has dual peaks because the centres of two EIT eigenmodes do not overlap. In the regime where $\Gamma_c > |\Delta_0|$, the extracted EIT spectra have dual linewidths because they are a superposition of two EIT eigenmodes with the same line centre but different linewidths. Indeed, we found that, without introducing a second (slightly tilted) Lorentzian with a different linewidth, a single-linewidth Lorentzian does not fit the experimental data well. As displayed in Figs 2 and 3 in the main text, our theory is in excellent agreement with the experimentally extracted data. The coupling rate Γ_c between the two channels is deduced from the phase-transition point by tuning $|\Delta_0|$, and the theoretical model for calculating Γ_c is under development.

Data availability. The data that support the plots within this paper and other findings of this study are available from the corresponding authors upon reasonable request.

References

51. Xiao, Y., Novikova, I., Phillips, D. F. & Walsworth, R. L. Diffusion-induced Ramsey narrowing. *Phys. Rev. Lett.* **96,** 043601 (2006).

52. Xiao, Y., Novikova, I., Phillips, D. F. & Walsworth, R. L. Repeated interaction model for diffusion-induced Ramsey narrowing. *Opt. Express* **16,** 14128–14141 (2008).
53. Klein, M., Hohensee, M., Phillips, D. F. & Walsworth, R. L. Electromagnetically induced transparency in paraffin-coated vapor cells. *Phys. Rev. A* **83,** 013826 (2011).
54. Xu, Z., Qu, W., Gao, R., Hu, X. & Xiao, Y. Linewidth of electromagnetically induced transparency under motional averaging in a coated vapor cell. *Chinese Phys. B* **22,** 033202 (2013).
55. Budker, D. *et al*. Microwave transitions and nonlinear magneto-optical rotation in anti-relaxation-coated cells. *Phys. Rev. A* **71,** 012903 (2005).